10.1 Numerical errors in flow over steep topography: analysis and alternatives

Katherine A. Lundquist[1]*, Fotini K. Chow[2], and Julie K. Lundquist [3]
[1] Lawrence Livermore National Laboratory, Livermore, CA
[2] University of California, Berkeley, CA
[3] University of Colorado, Boulder, CO

1 INTRODUCTION

It is well known in computational fluid dynamics that grid quality affects the accuracy of numerical solutions [Lee and Tsuei, 1992, You et al., 2006]. When assessing grid quality, properties such as aspect ratio, orthogonality of coordinate surfaces, and cell volume are considered. Mesoscale atmospheric models generally use terrain-following coordinates with large aspect ratios near the surface. As high resolution numerical simulations are increasingly used to study topographically forced flows, a high degree of non-orthogonality is introduced, especially in the vicinity of steep terrain slopes. Numerical errors associated with the use of terrain-following coordinates can adversely effect the accuracy of the solution in steep terrain. Inaccuracies from the coordinate transformation are present in each spatially discretized term of the Navier-Stokes equations, as well as in the conservation equations for scalars. In particular, errors in the computation of horizontal pressure gradients [Janjić, 1977, 1989], diffusion [Zängl, 2002, 2003], and horizontal advection [Schär et al., 2002] terms have been noted in the presence of sloping coordinate surfaces and steep topography.

In this work we study the effects of these spatial discretization errors on the flow solution for three canonical cases: scalar advection over a mountain, an atmosphere at rest over a hill, and forced advection over a hill. This study is completed using the Weather Research and Forecasting (WRF) model. Simulations with terrain-following coordinates are compared to those using a flat coordinate, where terrain is represented with the immersed boundary method [Lundquist et al., 2010]. The immersed boundary method is used as a tool which allows us to eliminate the terrain-following coordinate transformation, and quantify numerical errors through a direct comparison of the two solutions. Additionally, the effects of related issues such as the steepness of terrain slope and grid aspect ratio are studied in an effort to gain an understanding of numerical domains where terrain-following coordinates can successfully be used and those domains where the solution would benefit from the use of the immersed boundary method.

2 NUMERICAL METHOD

2.1 DESCRIPTION OF NUMERICAL ERRORS IN TERRAIN-FOLLOWING COORDINATES

Terrain-induced mesoscale systems include features such as sea and land breezes, mountain-valley winds, urban circulations, and forced advection over topographic obstacles [Pielke, 1984]. Terrain is frequently represented in mesoscale models by mapping the vertical coordinate to the terrain. The most frequently used mapping function defined by $\bar{z}$ or σ,

$$\bar{z} = \sigma = \frac{z_{top}(z - z_{ht}(x,y))}{z_{top} - z_{ht}(x,y)}, \tag{1}$$

was first proposed by Gal-Chen and Somerville [1975], where the overbar denotes the quantity in the transformed coordinate, z_{top} is the top of the domain, and $z_{ht}(x,y)$ is the terrain height. This function maps a domain with an irregular lower boundary onto a Cartesian grid, thereby simplifying the application of lower boundary conditions. Due to this advantage, this mapping function (or similar variants based on pressure or potential temperature and those using a non-dimensional formulation) is utilized in most modern mesoscale models. The disadvantage of this coordinate transformation is that it introduces additional terms into the governing equations. For example, the covariant velocity vectors which are perpendicular to coordinate sur-

---

Corresponding author address: Katherine A. Lundquist, Lawrence Livermore National Laboratory, P.O. Box 808, L-103, Livermore, CA 94551, email: kal@llnl.gov faces are given by equation 2.

$$\begin{pmatrix}\bar{u}\\ \bar{v}\\ \bar{w}\end{pmatrix} = \begin{pmatrix}1 & 0 & \frac{z_{top}-\bar{z}}{z_{top}}\frac{\partial z_{ht}}{\partial x}\\ 0 & 1 & \frac{z_{top}-\bar{z}}{z_{top}}\frac{\partial z_{ht}}{\partial y}\\ 0 & 0 & \frac{z_{top}-z_{ht}}{z_{top}}\end{pmatrix}\begin{pmatrix}u\\ v\\ w\end{pmatrix} \tag{2}$$

The extra terms are not difficult to handle numerically, as long as the transformation is well-behaved. As noted by Gal-Chen and Somerville this transformation is only well-behaved for terrain with continuous second derivatives, and when the determinant of the Jacobian ($\frac{z_{top}-z_{ht}}{z_{top}}$) is close to unity. Therefore, there is a wide variety of terrain, for which this transformation should not be used.

Inaccuracies from the coordinate transformation are present in each spatially discretized term of the Navier-Stokes equations, and arise from truncation errors due to the coordinate transformation (including both grid stretching and skewness) as well as the numerical calculation of the metric terms. Schär et al. [2002] carried out a theoretical analysis of truncation errors in a generalized transformed coordinate. The analysis considers the transformed one-dimensional advection equation:

$$\frac{\partial \rho}{\partial t} + J\frac{\partial(\rho u)}{\partial \bar{x}} = 0. \tag{3}$$

Here $J = \partial\bar{x}/\partial x$ is the Jacobian of the transformation, where the overbar indicates the transformed coordinate.

After applying a Taylor series expansion, the error term is derived in computational space. Using the transformation back to physical space ($\Delta\bar{x} = J\Delta x$), the total truncation error for a first order upwind scheme is given by equation 4.

$$E = \frac{\Delta x}{2}J\frac{\partial}{\partial x}\left(uJ^{-1}\frac{\partial \rho}{\partial x}\right) + O(\Delta x^2) \tag{4}$$

Applying the chain rule, the truncation error may be split into two parts given in equation 5. E_{fd} is attributed to the finite differencing scheme, and E_t to the coordinate transformation.

$$E_{fd} = \frac{\Delta x}{2}\frac{\partial}{\partial x}\left(u\frac{\partial \rho}{\partial x}\right) + O(\Delta x^2) \tag{5a}$$

$$E_t = -\frac{\Delta x}{2}u\frac{\partial \rho}{\partial x}J^{-1}\frac{\partial J}{\partial x} + O(\Delta x^2) \tag{5b}$$

It is seen here that the leading term for the error due to each cause is of the same order of magnitude O(Δx). Thus, large Jacobian terms as well as large gradients in the Jacobian lead to significant increases in the transformation truncation error. In the limit of the Jacobian approaching unity, the truncation error reduces to the theoretical form from the finite differencing scheme. At this point the Jacobian is in an exact form. Numerical estimates of the Jacobian using finite differencing include additional truncation errors.

Furthermore, Mahrer [1984] notes that numerically inconsistent horizontal derivatives arise when the distance between two vertical grid points (Δz) is smaller than the elevation difference between two horizontally adjacent points. This inconsistency occurs even when the metric term is included in the calculation (computing horizontal gradients along sloping surfaces without consideration for the metric terms is also commonplace). Additionally, the common practice of stretching the grid towards the bottom boundary to achieve fine vertical resolution near the surface, exacerbates these errors. In the transformed coordinate, a horizontal derivative is calculated as:

$$\left.\frac{\partial}{\partial x}\right|_z = \left.\frac{\partial}{\partial x}\right|_{\bar{z}} + \left.\frac{\partial \bar{z}}{\partial x}\right|_z\frac{\partial}{\partial \bar{z}}. \tag{6}$$

In a forward finite differencing scheme, this derivative is approximated as:

$$\begin{aligned}\left.\frac{\partial F}{\partial x}\right|_z = &\frac{F(i+1,j)-F(i,j)}{\Delta x}\\ &+\left.\frac{\partial \bar{z}}{\partial x}\right|_{i,j}\frac{F(i+1,j+1)-F(i+1,j)}{\Delta \bar{z}}.\end{aligned} \tag{7}$$

The stencil used in this finite difference scheme is shown in figure 1. It can clearly be seen that for a true horizontal derivative in physical space, it would be more appropriate to use the computational points located at $F(i+1, j+3)$ and $F(i+1, j+4)$. Mahrer [1984] demonstrated a reduction in errors when using this modified stencil.

Geometrically, these errors are more likely to occur at large aspect ratios, when the horizontal grid spacing is much larger than the vertical grid spacing, making it more common for the vertical change in height over the horizontal grid spacing to be larger than the vertical grid spacing of the computational cell. This point is illustrated in figure 2, which depicts the skewness of computational cells as a function of terrain slope and aspect ratio. The gray area delineates the parameter space where numerical inconsistencies occur in horizontal derivatives because the change in grid height over one Δx is larger than the vertical grid spacing Δz. In practice, mesoscale modelers often stretch the grid towards the surface, using very large grid aspect ra-

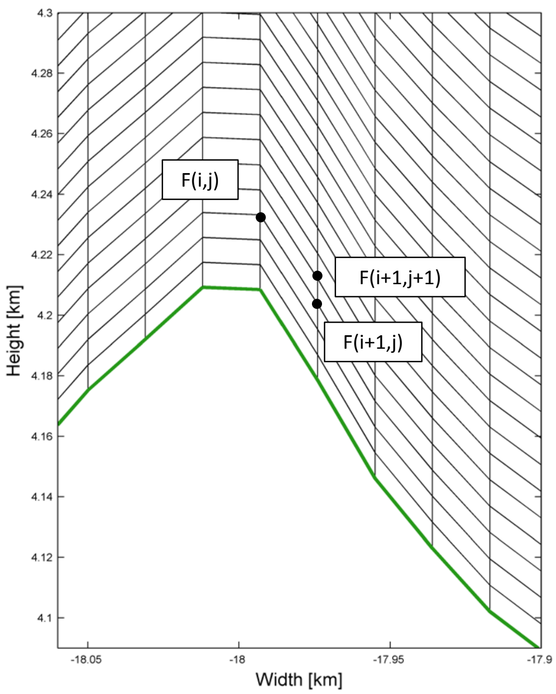

Figure 1: A schematic of the stencil used in a forward finite difference approximation of a horizontal derivative.

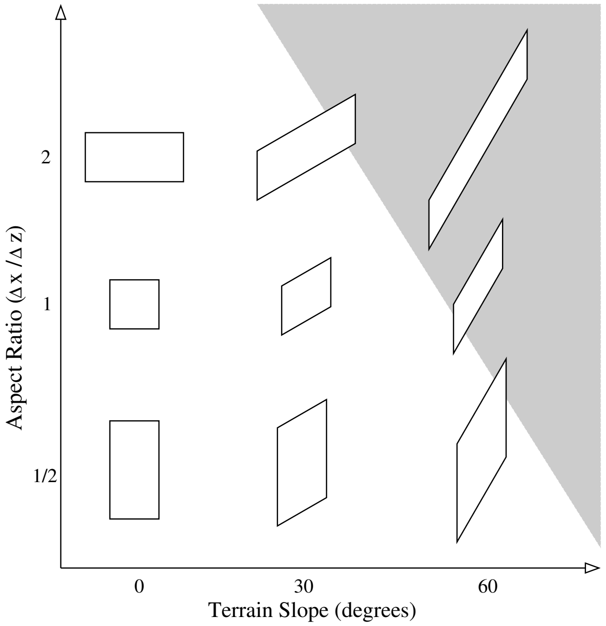

Figure 2: The magnitude of errors arising from the use of terrain-following coordinates is a function of terrain slope and aspect ratio. Example computational cells are shown at a variety of terrain slopes and aspect ratios. The shaded region denotes the parameter space where the use of terrain-following coordinates is questionable because the change in height over two horizontally adjacent points is larger than the vertical grid spacing Δz.

tios. For example, a grid with 1 km horizontal spacing may have the first vertical grid point located at 50 m, leading to an aspect ratio of 20. From experience most modelers believe that the use of terrain-following coordinates is limited to approximately 30 degree slopes, however, at an aspect ratio of 20 the guidelines of Mahrer are violated with just a 2.9 degree terrain slope. This plot shows that decreasing the aspect ratio or horizontal grid spacing (Δx) can reduce these errors. It is clear that common practice is not in line with the current understanding of numerical errors, thus warranting further study.

2.2 *ALTERNATIVE GRIDDING TECHNIQUES*

Several methods have been proposed to reduce the truncation error arising from terrain-following coordinates. Schär et al. [2002] proposed a modified sigma coordinate in terms of height in which grid distortion due to small scale terrain features decays with height more rapidly than distortion caused by large scale features. The modified coordinate flattens quickly, reducing grid skewness with height, and improves the accuracy of the solution. Zängl [2003] extended this method to pressure based coordinates. Klemp et al. [2003] investigated the errors that arise when numerical treatment of the metric terms is inconsistent with the discretization of other terms in the governing equations. Distortion seen in topographically induced gravity waves was reduced with consistent numerical treatment.

Several alternatives to terrain-following coordinates exist. One method is fitting the topography to Cartesian coordinates, thereby creating a zeroth order stepwise representation of the terrain. Additionally, structured or unstructured body-fitted coordinates are often employed for meshing in complex geometries. Another solution is the use of structured or Cartesian grids which do not align or conform with the geometries to be represented. With non-conforming grids the geometry or boundary passes through the computational domain, and boundary conditions are assigned within the domain, rather than on domain edges. Adcroft et al. [1997] used a shaved cell approach to represent topography on a Cartesian grid. This method eliminates grid distortion, but introduces complications in the numerical solution at the ground because the computational cells must be modified (shaved) where they intersect the topography. The immersed boundary method [Iaccarino and Verzicco, 2003, Mittal and Iaccarino, 2005] is another non-conforming grid option. In this method an artificial force field is imposed at computational nodes near the boundary to represent the effects of the boundary. Interpolation of the force field is used to enforce the boundary conditions directly on the boundary (which does not align with computational nodes), rather than modifying the computational cell as in shaved cell methods. The immersed boundary method has been implemented in WRF [Lundquist et al., 2010], and is used in this study to examine the role that grid quality plays in high-resolution atmospheric modeling over complex terrain.

2.3 METRIC TERMS IN THE GOVERNING EQUATIONS

The mesoscale model WRF solves the non-hydrostatic compressible Euler equations which have been transformed into a pressure-based terrain-following coordinate. Two coordinate transformations are required for the vertical coordinate. The first transforms the equations into the hydrostatic pressure coordinate, and the second transforms the equations into the terrain-following coordinate. An additional velocity is introduced in these transformations, and is defined as the contravariant velocity of the vertical coordinate $\dot{\eta}$. Therefore, WRF solves the transformed Navier-Stokes equations plus an additional equation representing $\dot{\eta}$. The coordinate velocity is relevant here because the definition contains terms from the Jacobian matrix for the coordinate transformation. The equation defining $\dot{\eta}$ is rearranged so that it appears in WRF as a prognostic equation for the geopotential ϕ. The transformed equations are given by:

$$\partial_t \mu + \nabla \cdot (\mu \vec{V}) + \partial_\eta (\mu \dot{\eta}) = 0 \tag{8a}$$

$$\begin{aligned} \partial_t (\mu \vec{V}) + \nabla \cdot (\mu \vec{V}; \vec{V}) + \partial_\eta (\mu \dot{\eta} \vec{V}) \\ - \nabla (p \partial_\eta \phi) + \partial_\eta (p \nabla \phi) = \vec{F} \end{aligned} \tag{8b}$$

$$\begin{aligned} \partial_t (\mu w) + \nabla \cdot (\mu \vec{V} w) + \partial_\eta (\mu \dot{\eta} w) \\ - g \left(\partial_\eta p - \mu \right) = F \end{aligned} \tag{8c}$$

$$\partial_t \phi + \vec{V} \cdot \nabla \phi + \dot{\eta} \partial_\eta \phi - g w = 0. \tag{8d}$$

In the above equations $\vec{V}$ only includes horizontal velocities, and ∇ operates on coordinate surfaces in the horizontal dimension. Geopotential is defined as $\phi = gz$, so that $\nabla \phi$ and $\partial_\eta \phi$ are surrogates for the Jacobian terms ∇z and $\partial_\eta z$.

Terms created by the change of coordinates may be evaluated analytically if the terrain function is differentiable and the Jacobian matrix is invertible. Instead it is often more practical to compute the metric terms numerically, as is the case in WRF. The Jacobian maps the physical topography onto a rectangular domain, and in WRF the terms are also affected by movement of the vertical coordinate during the time integration. Therefore, the Jacobian terms appearing in WRF must be evaluated numerically at each time step (making an analytical evaluation impractical). The terms are evaluated with an even-order finite difference scheme that is greater than or equal to the order of the advection scheme. Advection schemes range from 2nd to 6th order, therefore if a 3rd or 4th order advection scheme is used, the Jacobian terms are evaluated with a 4th order scheme.

When the immersed boundary method is used, the coordinates are still changed into pressure coordinates, but the transformation to terrain-following coordinates is eliminated. Horizontal gradients of the coordinate are substantially reduced with IBM, but the magnitude of the gradients may not be exactly zero due to time variability of the grid arising from the transformation to pressure coordinates.

3 ANALYSIS OF NUMERICAL ERRORS

First, two cases with analytical solutions are chosen to quantify numerical errors and demonstrate the increased accuracy of the simulations using the immersed boundary method over terrain-following coordinates. The first is an idealized advection test similar to those presented by Schär et al. [2002] and Zängl [2003], demonstrating improved horizontal advection far above steep topography. The second is an atmosphere at rest over an isolated hill, following Zängl [2003] and Zängl et al. [2004], quantifying errors primarily in the calculation of horizontal gradients in the diffusion terms. Forced flow over a topographic obstacle (a hill) is included as a third case. This case is used to assess the effects of terrain slope, grid aspect ratio, and turbulent viscosity on solutions using terrain-following coordinates.

3.1 IDEALIZED ADVECTION OF A SCALAR

In the scalar transport test case of Schär et al. [2002], highly variable topography (with a maximum slope of 49 degrees) resides in a quiescent air mass, with a uniform flow aloft, as shown in figure 3. A shear layer in the velocity sounding persists without mixing due to the absence of viscosity. The

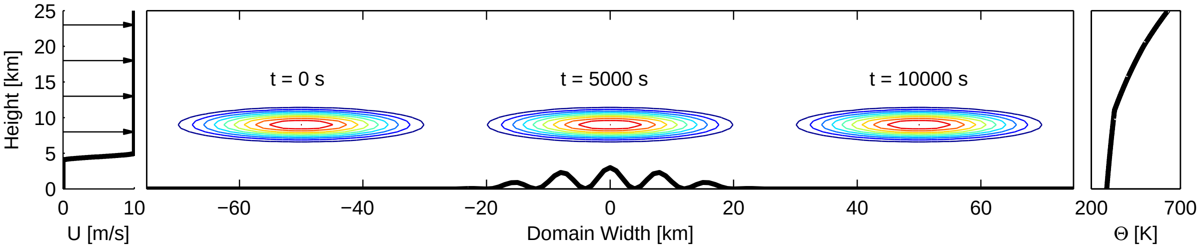

Figure 3: Set-up of the idealized advection test from Schär et al. [2002]. Topography is submerged within a stagnant air mass, with uniform flow above. Temperature is initialize as that of a standard atmosphere. The analytic solution is shown for advection of a scalar cloud at three different times.

shear layer isolates the effects of the terrain from the flow aloft, so that when a scalar anomaly is introduced it advects over the terrain without distortion or diffusion. The analytical solution for the advection of a scalar cloud is presented in figure 3 at three different times. In the simulations presented here, potential temperature is initialized as that of a standard atmosphere which specifies the stable temperature profile shown in figure 3. A standard atmosphere was also used in the simulations of Zängl [2003]=, although the analytical solution is independent of the background temperature profile. Simulations of this case with a neutral atmosphere can be found in Lundquist et al. [2008]. When terrain-following coordinates are used, the horizontal grid lines retain the signature of the topographic features. Discretization of the terrain-following coordinates leads to an additional truncation error which is a function of the Jacobian. These truncation errors cause distortion of the scalar as it advects through the domain as illustrated below.

3.1.1 Model set-up and initialization

In this test, the topography is specified as the product of two oscillatory functions. The first function has a large-scale wavelength of 50 km, and the second perturbation function has a wavelength of 8km. The equation for the topography is given as:

$$h_x(x) = \begin{cases} h_o \cos^2(\frac{\pi x}{2a}) \cos^2(\frac{\pi x}{\lambda}) & \text{for } |x| \leq a \\ 0 & \text{for } |x| > a \end{cases} \tag{9}$$

where h_o = 3 km, a = 25 km, and λ = 8 km.

Velocity, potential temperature, and water vapor mixing ratio are specified with a vertical sounding. Velocity is specified by:

$$u(z) = \begin{cases} u_o & \text{for } z > z_2 \\ u_o \sin^2(\frac{\pi}{2} \frac{z - z_1}{z_2 - z_1}) & \text{for } z_1 \leq z \leq z_2 \\ 0 & \text{for } z < z_1 \end{cases} \tag{10}$$

where u_o = 10 m s^{-1}, z_1 = 4 km, and z_2 = 5 km. The atmosphere is stable, with a potential temperature of 288 K at sea level, a tropospheric vertical temperature gradient of -6.5 K km^{-1}, and an isothermal atmosphere above the tropopause at a height of 11 km. A dry atmosphere is considered.

The total domain size is (X, Y, Z) = (300 km, 2 km, 25 km) for the simulation with terrain-following coordinates. When the immersed boundary method is used, the domain is extended 1 km in the vertical dimension to (X, Y, Z) = (300 km, 2 km, 26 km). The vertical domain ranges from -1 km to 25 km, allowing for computational nodes below the zero terrain height. These extra nodes are used as forcing points in the immersed boundary method. The number of grid points in the terrain-following coordinate case is (n_x, n_y, n_z) = (301,3,51), and with the immersed boundary method it is (n_x, n_y, n_z) = (301,3,53). Horizontal resolution in the base case is $\Delta X = \Delta Y$ = 1 km, and vertical resolution is ΔZ = 0.5 km. The vertical coordinate is stretched in the pressure-based η coordinate, to maintain uniform spacing in physical space. The time step is Δt = 20 s. Schär et al. [2002] use a 25 s time step; however, a smaller time step of 20 s is needed in WRF to achieve numerical stability.

The scalar cloud is defined by equation 11, where the maximum amplitude is φ_o = 1, the horizontal half width is A_x = 25 km, and the vertical half width is A_z

= 3 km.

$$r = \left[\left(\frac{x - x_o}{A_x} \right)^2 + \left(\frac{z - z_o}{A_z} \right)^2 \right]^{1/2} \tag{11a}$$

$$\varphi(x,z) = \begin{cases} \varphi_o \cos^2(\frac{\pi r}{2}) & \text{for } r \leq 1 \\ 0 & \text{for } r > 1 \end{cases} \tag{11b}$$

The scalar is initialized at the location (X_o, Z_o) = (-50 km, 9 km). It is centered in the domain at t = 5000 s, and the center is located at (X_o, Z_o) = (50 km, 9 km) when the time integration ends at t = 10000 s.

Schär et al. solved the advection-diffusion equation, but specified the underlying velocities. Zängl [2003] examined the case when the momentum equations are solved in addition to the advection-diffusion equation using the MM5 mesoscale model. In our simulations, the momentum equations are solved, along with advection-diffusion of potential temperature and the passive scalar cloud. Comparisons with the analytical solution are made with numerical simulations using standard terrain-following coordinates and those using IBM. Default WRF options are used, and include a 3rd order Runge Kutta time stepping scheme, 5th order horizontal advection, and 3rd order vertical advection. The odd-order advection schemes are upwind-biased and diffusive. Default constants are used for filtering in time, and include a divergence damping coefficient γ_d = 0.1, external mode damping coefficient γ_e = 0.01, and acoustic time step off-centering of β = 0.1.

Large truncation errors are present in the native coordinate, and it is demonstrated that the immersed boundary method can be used within WRF to alleviate these errors. Truncation errors can be attributed to either the finite differencing scheme for advection or the coordinate transformation. By comparing the solutions on the terrain-following and immersed boundary grids, the magnitude of error attributable to each cause is assessed.

3.1.2 Results

Figure 4 shows contours of u and w velocity at t = 10000 s, with results using terrain-following coordinates on top, and those using IBM below. In the analytical solution there is no interaction with the topography, and the velocity field is specified by equation 10 at all times. When terrain-following coordinates are used it is clear that the distortion of the grid makes it impossible to isolate the flow aloft from terrain effects. Waves, induced by errors in the coordinate transformation, form above the mountain range. Horizontal velocity should range from 0 to 10 m s^{-1}, and vertical velocity should remain zero. However, horizontal velocities of -0.53 to 11.72 m s^{-1} and vertical velocities of -0.59 to 0.65 m s^{-1} are present. Errors in the velocity field for the WRF case are much larger than when IBM is used, where the error is negligible. At the end of the IBM simulation, horizontal velocity ranges between -2.27e-4 and 10.0003 m s^{-1}, and vertical velocity between -1.63e-4 and 1.37e-4 m s^{-1}.

Errors for this simulation (using terrain-following coordinates and a stable atmosphere) are larger than seen by Zängl [2003] using the native MM5 terrain-following coordinate. While Schär et al. prescribed the velocity field (and therefore we can not compare our velocity results to theirs), Zängl allowed the velocity to evolve. Zängl reported maximum vertical velocities of 0.19 m s^{-1} using the native MM5 coordinate. One possible reason why his results are much better than the WRF results using the native coordinate may be due to the model set-up. The topography used in the Zängl simulation was shorter and wider than in the original Schär et al. set-up, leading to less distortion of the grid, and the shear velocity layer spanned a larger distance, allowing additional resolution. Zängl reported vertical velocities of 0.02 m s^{-1} using the alternate gridding approach of a modified SLEVE coordinate that flattens quickly with height, which is more error than seen in our simulations when our alternative gridding approach using the immersed boundary method is used.

Snapshots of the scalar cloud are included in figure 5, along with the associated errors. Significant distortion of the scalar anomaly occurs as it advects over the terrain features in the simulation with sigma coordinates. At the last time the shape of the cloud is not only distorted, but the center of the cloud has advected 0.5 km less than in the analytical solution. Error is calculated as the difference between the numerical and analytical solution, and is shown with contour intervals of 0.01. At the last time shown, error for the WRF solution ranges from -0.183 to 0.191, while the scalar concentration ranges from -0.183 to 0.827. In the simulation using the immersed boundary method, distortion of the cloud is eliminated. No contours appear in the IBM-WRF error plot, because the error is less than the threshold of the first contour (0.01).

Errors in the IBM-WRF simulation are included in figure 6 with appropriate contour levels (intervals are at 1e-4). In IBM-WRF the deviation from the analytical solution ranges from -7e-4 to 7e-4,

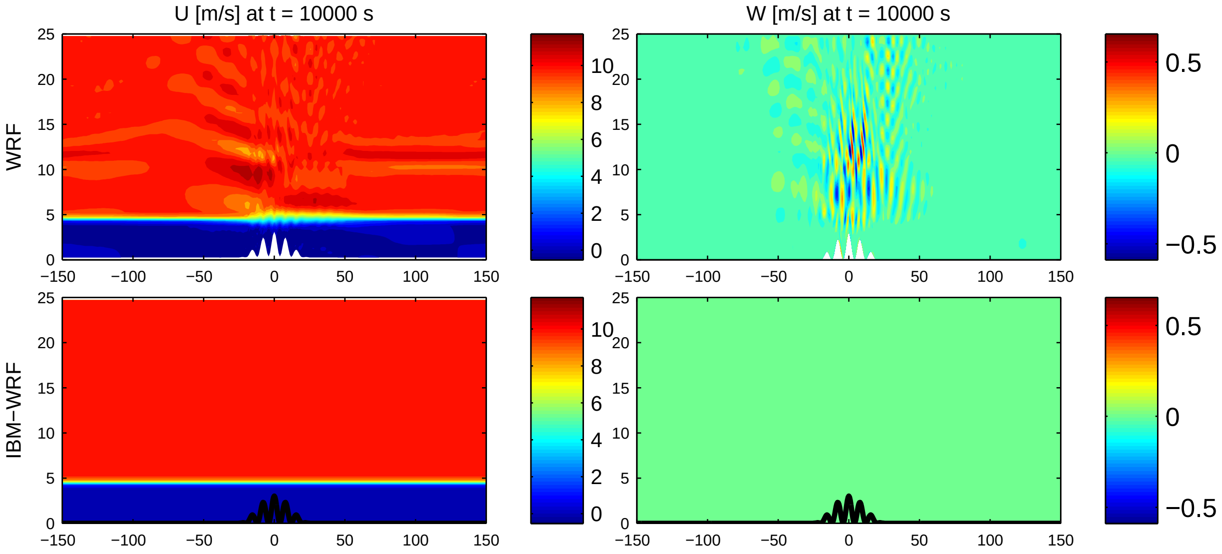

Figure 4: Contours of the u and w components of velocity in m s^{-1} for terrain-following coordinates (top) and the immersed boundary method (bottom) at t = 10000 s. In the analytical solution, the velocity should equal the initial sounding throughout the duration of the simulation. Axes indicate domain size in km, and are not to scale.

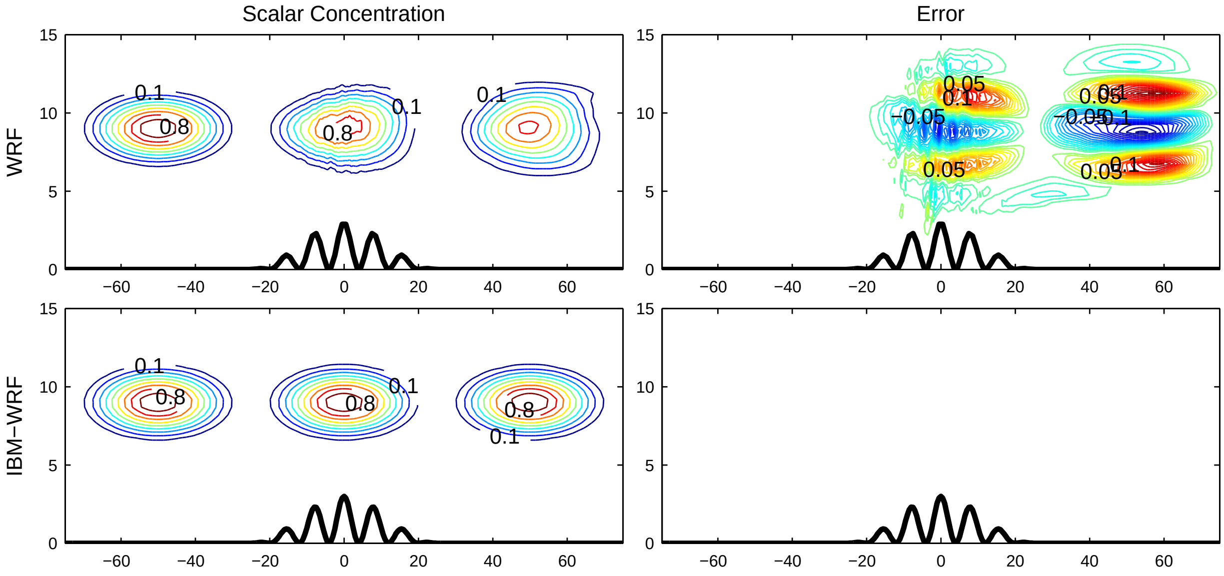

Figure 5: On the left, the scalar concentration is shown at t = 0, 5000, and 10000 s. Scalar units are non-dimensional with a range of 0 to 1. Contour intervals are in 0.1 increments. Error is shown on the right, and is calculated as the difference between the numerical and analytical solutions. Contour intervals are 0.01. Error for the IBM-WRF simulation is less than the first contour level (see figure 6 for IBM-WRF error). The zero contour is suppressed. Axes indicate domain size in km, and are not to scale.

Table 1: Summary of errors for the scalar φ at t = 10000 s for the WRF simulations with the default advection scheme and those presented in Schär et al. [2002] and Zängl [2003] (at t = 4 hours). Analytical values of φ_{min} and φ_{max} are 0 and 1. $\Delta\varphi$ is the difference between the numerical and analytical solutions.

Coordinate	Order of Advection Scheme	φ min	φ max	$\Delta\varphi$ min	$\Delta\varphi$ max
WRF Sigma	h:5th, v:3rd	-0.183	0.827	-0.183	0.191
Schär et al. Sigma	1st	0.000	0.284	-0.700	0.213
	2nd	-0.168	0.953	-0.174	0.162
	4th	-0.058	1.001	-0.057	0.052
Zängl Sigma	2nd	n/a	n/a	-0.12	0.10
IBM-WRF	h:5th, v:3rd	-6e-12	0.988	-7e-4	7e-4
Schär et al. No Topography	1st	0.000	0.762	-0.220	0.141
	2nd	-0.023	0.985	-0.023	0.021
	4th	-0.002	0.984	-0.002	0.002
Zängl No Topography	2nd	n/a	n/a	-0.02	0.02

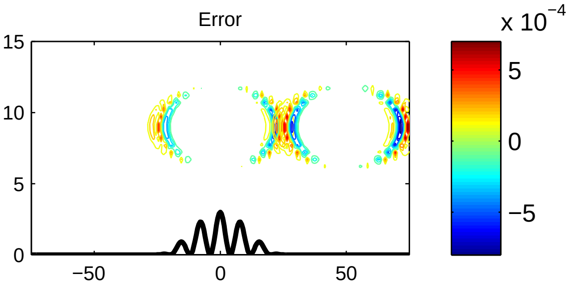

Figure 6: Error is shown for the immersed boundary method case at t = 0, 5000, and 10000 s. Contour intervals are 1e-4. The zero contour is suppressed. Axes indicate domain size in km, and are not to scale.

with scalar values ranging from -6e-12 to 0.988. These errors are identical to those which appear if no topography is present, and can be attributed to the finite differencing scheme. In Lundquist et al. [2008], IBM-WRF simulations were produced using 3rd through 6th order advection schemes, and it was shown that error decreased as the order of the finite difference increased, while this was not the case when terrain-following coordinates were used and large errors were present despite the order of the spatial discretization. The results of these simulations indicate that the truncation error is dominated by the term arising from the transformation to terrain-following coordinates, and errors from the pressure coordinate transformation and the finite differencing scheme are negligible.

Again, errors in the scalar field for the WRF simulation are larger than in Zängl [2003], where errors in scalar concentration ranged from -0.12 to 0.10 with a stable atmosphere. A comparison of the WRF and IBM-WRF results and those presented in Schär et al. [2002] and Zängl [2003] is included in table 1. Schär et al. published results for simulations with 1st, 2nd, and 4th order advection schemes (among others which are not included here). For reference, both papers also included a set of simulations with no topography. Error in the reference simulations is exclusively caused by the finite differencing schemes. The simulations without topography could be viewed as comparable to the IBM-WRF simulations because the coordinate surfaces of the grid are flat in both cases. As expected, higher order advection schemes decrease error for both sigma coordinates and the reference cases of Schär et al.. The IBM-WRF simulation (with topography) performs as well or better than the 4th order reference case with no topography. This is a logical result, as the immersed boundary method alleviates the need for a coordinate transformation and the simulations use a similar order of accuracy in the advection schemes.

Schär et al. cite several causes of error in the idealized advection tests, first reasoning that, “Schemes with implicit diffusion suffer particularly large coordinate transformation errors. Diffusion spreads out the solution in computational space, rapidly broadens the initial anomaly, and thereby makes the scheme more susceptible to coordinate transformations.” In a grid refinement study, Schär et al. found that the solution was extremely sensitive to horizontal resolution, and large gains in accuracy could be achieved through increased horizontal resolution. The solution was shown to be

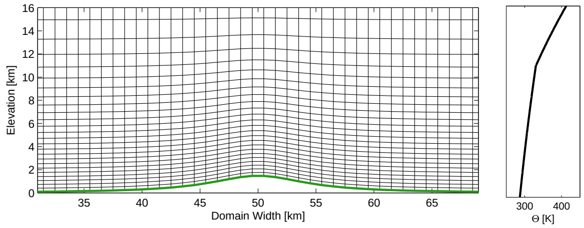

Figure 7: The mountain terrain, along with the grid for terrain-following coordinates is shown. Every other vertical coordinate surface is shown for clarity. This hill has a maximum slope of approximately 10 degrees. Potential temperature is initialized with a sounding (shown on the right) which specifies that of a standard atmosphere.

insensitive to vertical resolution. This may be because increasing the horizontal resolution reduced the grid aspect ratio, and therefore reduced numerical inconsistencies in the finite difference schemes, as noted by Mahrer [1984], and illustrated in figures 1 and 2. Additionally, as shown in table 1, Schär et al. found that increasing the order of the advection scheme had a beneficial impact on the quality of the solution. Accuracy was largely gained from an increase in the order of the horizontal scheme, whereas the vertical scheme had little effect.

3.2 ATMOSPHERE AT REST

The second case used to evaluate errors due to terrain-following coordinates is an atmosphere at rest over an isolated mountain [Zängl, 2003, Zängl et al., 2004]. In this case, a dry, stable, and quiescent atmosphere resides over a three-dimensional hill. The set-up is shown in figure 7, which includes the terrain-following grid at the peak of the hill in the center of the domain and the vertical profile of potential temperature. In the absence of forcing (at the surface or otherwise), the atmosphere should remain at rest, however, flow can be induced by numerical errors. While only a dry atmosphere is considered here, Zängl et al. [2004] demonstrated that when moist physics are included these numerical errors can induce substantial amounts of spurious precipitation over steep mountains.

3.2.1 Model set-up and initialization

The mountain height h_t is specified as a three dimensional hill, given by:

$$h_t(x,y) = \frac{h_p}{1 + (x/a)^2 + (y/a)^2}, \qquad (12)$$

with a peak height h_p of 1500 m and a half-width a of 5 km. In contrast to the steep and highly variable terrain used in the previous case, the terrain in this case is smooth with shallow slopes, and a maximum slope of approximately 10 degrees. At initialization, the atmosphere is specified as quiescent, dry, and with the potential temperature profile of a standard atmosphere, as previously described in section 3.1. Pressure is initialized to be in hydrostatic balance with the temperature field. Atmospheric physics, other than parameterized turbulent mixing, are not used.

The domain has (n_x, n_y, n_z) = (101,101,50) grid points with terrain-following coordinates, and (n_x, n_y, n_z) = (101,101,55) grid points when the immersed boundary method is used. Both grids have a horizontal grid spacing of Δx = Δy = 1 km. A rigid lid is specified at the domain top of 16 km. Spacing in the vertical grid is constant in the pressure coordinate η, but stretched in physical space. At initialization, the minimum vertical grid spacing is 147.4 m with a maximum of 1048.5 m for the terrain-following grid. For the immersed boundary grid, the minimum and maximum vertical grid spacing is 143.8 m and 1017.8 m. A time step of Δt = 6 s is used. Periodic boundary conditions are specified at the lateral domain edges. Second order explicit diffusion is used. Historically, horizontal gradients for the diffusive terms were often calculated along sloping coordinate surfaces, and the metric terms were neglected. Several researchers [Janjić, 1977, 1989, Schär et al., 2002, Zängl, 2002, 2003] demonstrated numerical errors related to the simplification of calculating gradients along sloping surfaces. Therefore, WRF also includes the option to include the metric terms of the coordinate transformation in the calculation of the diffusive terms. This improves results, but as pointed out in Mahrer [1984], when the change in grid height over one Δx exceeds the vertical grid spacing Δz, inclusion of the metric terms still will not yield a truly horizontal calculation of the gradient. Both options, diffusion along coordinate surfaces as well as including the metric terms, are considered in this section. Additionally, simulations using the immersed boundary method are presented. In all cases the horizontal diffusion coefficient is set to 1000 m^2 s^{-1}, while vertical diffusion is not specified. While the coefficient used for horizontal diffusion is quite large, it is comparable to the coefficients used in Zängl [2003] and Zängl et al. [2004], and allows direct comparisons with the MM5 results presented in those works.

3.2.2 Results

The solution is integrated for a time period of 24 hours. Contours of potential temperature and velocity magnitude are shown at the end of the simulation in figure 8. Isentropes should remain completely horizontal and undisturbed during the simulation. While the contour lines appear relatively flat, there is moderate distortion of the vertical potential temperature gradient, especially very near the surface in the simulation with diffusion along coordinate surfaces, and near the height of the tropopause in both simulations with terrain-following coordinates. At the tropopause, there is a discontinuity in the vertical temperature gradient. Numerical errors are introduced in this region as the grid height varies in the horizontal due to sloping terrain-following coordinates, and finite difference calculations of the horizontal gradient are inconsistent. Lesser errors are seen outside of the tropopause because the temperature profile is linear in these regions. The constant vertical gradient reduces errors in the calculation of horizontal gradients in sloping terrain (by eliminating errors in the calculation of the vertical gradient). Errors in the temperature and pressure fields induce flow. At the end of the simulation the maximum velocity magnitude along the center line is 1.74, 0.28, and 3.8e-5 m s^{-1} for simulations with diffusion along coordinate surfaces, horizontal diffusion, and IBM respectively. Contours of velocity magnitude are shown in figure 8

Zängl [2003] found larger vertical velocities adjacent to the center line of the domain, noting that for MM5 simulations with 4th order diffusion along coordinate surfaces vertical velocities of 1.5 m s^{-1} are present along the center line and increase to 3 m s^{-1} adjacent to the center line. We also found this to be the case in our simulations with maximum velocity magnitudes of 2.192, 0.318, and 5.5e-5 m s^{-1} present for the simulations with diffusion along coordinate surfaces, horizontal diffusion, and IBM when the entire domain is considered. Zängl notes that when horizontal diffusion is used, spurious air motions are limited to the tropopause (where there is a discontinuity in the vertical potential temperature gradient), while air motion extends throughout the domain when diffusion is calculated along coordinate surfaces. This is also true in our simulations, as seen in figure 8.

Table 2: Maximum value of the absolute value of individual velocity components [m s^{-1}] for the WRF simulations in the top rows of the table with comparisons to previous works in the bottom rows.[Zängl, 2003, Zängl et al., 2004] .

	u	v	w
WRF coordinate surf.	1.67	2.18	0.67
WRF horizontal	0.32	0.32	0.01
IBM-WRF	7e-5	7e-5	8e-5
MM5 coordinate surf.	n/a	n/a	0.44
KAMM2 horizontal	n/a	n/a	0.40

Zängl reported only vertical velocities, however, we found significant horizontal velocities in our simulations. The maximum norm of each velocity component is reported in table 2. The horizontal velocity components are much larger than the vertical velocities for the WRF cases with terrain-following coordinates. Velocities in all three directions are nearly eliminated by using the immersed boundary method. Zängl [2003] produced MM5 simulations with second order diffusion, in addition to those with fourth order diffusion. In the intercomparison study [Zängl et al., 2004] the model KAMM2 is used with second order diffusion to simulate this test case. Results for these simulations with second order diffusion can be directly compared to our results (which also use second order diffusion), and are included in table 2. Zängl notes that the errors for the simulations with second order diffusion are much smaller than than seen in simulations with fourth order diffusion. His MM5 simulation with second order diffusion along coordinate surfaces produced a maximum vertical velocity of 0.44 m s^{-1}, while our WRF simulation with diffusion along coordinate surfaces has a maximum vertical velocity of 0.67 m s^{-1}. The KAMM2 simulations with horizontal diffusion operators produced a maximum vertical velocity of 0.40 m s^{-1}, while WRF with horizontal diffusion produced vertical velocities of just 0.01 m s^{-1}.

3.3 FORCED ADVECTION OVER TOPOGRAPHY

3.3.1 Model set-up and initialization

The case of advection over a topographic hill feature driven by a geostrophic pressure gradient is used to examine the effects of terrain slope, grid aspect ratio, and viscosity by completing a series of

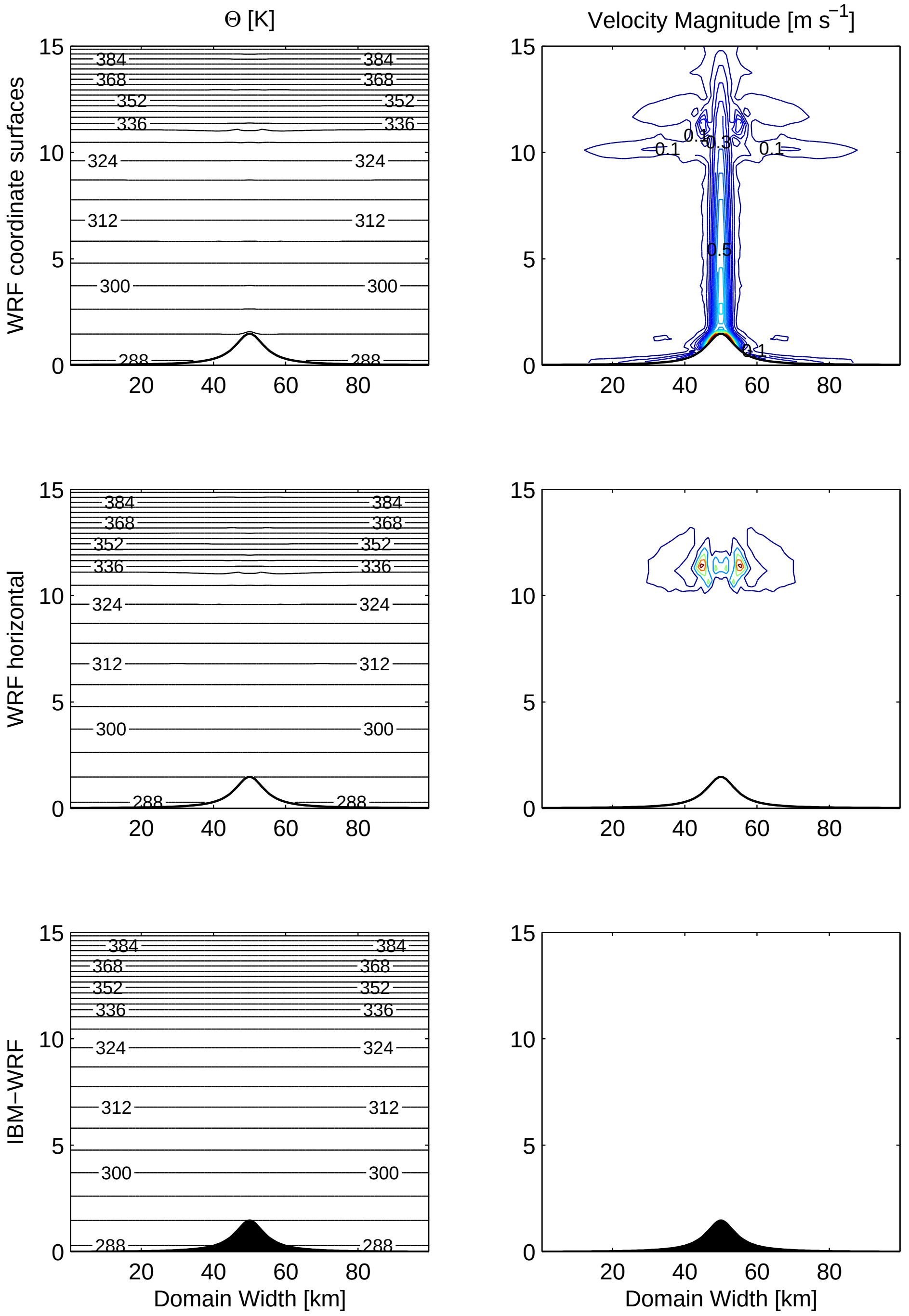

Figure 8: Contours of potential temperature [K] (right) and velocity magnitude [m s^{-1}] at 24 hours for the atmosphere at rest case. The top panels show simulation with simplified diffusion along coordinate surfaces, the middle panels include an evaluation of the metric terms of the coordinate transformation, and the simulation using the immersed boundary method is shown on the bottom. Contour intervals for potential temperature are 4 K and for velocity are 0.05 m s^{-1}.

simulations and varying these parameters. The terrain height of the three-dimensional hill is defined, as in the atmosphere at rest case, by equation 12 in the previous section, using three different peak mountain heights h_p of 218, 451, and 716 m and a constant mountain half-width a of 800 m to vary the maximum terrain slope. This geometry leads to a maximum slope of 10, 20, and 30 degrees. The flow is initialized with a neutral sounding of 288 K, so that the perturbation temperature is -12 K off of the base state of 300 K. Additionally, the sounding specifies a constant velocity of 10 m s^{-1} for u, and 0 m s^{-1} for v. The flow is driven by a pressure gradient that would balance a geostrophic wind of 10 m s^{-1} in the x direction. The Coriolis parameter f is set to a constant value of 1 x 10^{-4} s^{-1}. The number of grid points in the horizontal direction is (nx, ny) = (60,60), with a constant 100 m grid spacing. The top of the domain is located at a height of 4500 m, and in the vertical dimension the grid points are equally spaced in physical space, so that the grid spacing is either Δz = 50 m or Δz = 100 m (leading to an aspect ratio $\Delta x/\Delta z$ of 2 and 1). Additional points are used in the vertical direction when the immersed boundary method is used instead of terrain-following coordinates to account for the fact that nodes are needed underneath the terrain to enforce the boundary condition at the immersed surface. Therefore, the domain begins at z = -200 m in the IBM cases (rather than at z = 0 m in the terrain-following case), and four additional grid points are used in the vertical direction when Δz = 50 m, or two points when Δz = 100 m. A constant eddy viscosity of 20 or 30 m^2 s^{-1} is used.

Periodic boundary conditions are used at the lateral boundaries. A no-slip boundary condition is set on velocity at the terrain surface, along with a zero flux condition on temperature. At the top of the domain, the native WRF boundary condition is used (isobaric and a material surface), with a Rayleigh damping layer that acts only on vertical velocity at the top 500 m of the domain. The flow is integrated for 144 hours, allowing the inertial oscillations present in the solution to damp out so that the final solution can be considered steady. Results presented in the remainder of this section are instantaneous at a time of 144 hours.

3.3.2 Results

Profiles of each velocity component are shown in figures 9, 10, and 11 for several locations along the x dimension. Profiles for the 10 degree slope are shown in figure 9, the 20 degree slope in figure 10, and the 30 degree slope in 11. The left column of subfigures is along the center line of the domain, where $y \approx$ 3000 m, while the right column shows a slice at $y \approx$ 4500 m. The two black dashed lines show the WRF solution at the two different aspect ratios with Δz = 50 m or Δz = 100 m, while the red and blue lines show the IBM-WRF solutions at the same aspect ratio. It is interesting to note that the WRF solution appears to change with the two aspect ratios, while the IBM-WRF solution appears insensitive to aspect ratio. Additionally, both IBM-WRF solutions show fewer differences with the WRF solution with Δz = 50 m, regardless of the vertical grid spacing. More testing is needed to examine how aspect ratio and grid resolution effect the solution independently on the WRF terrain-following and IBM-WRF grids.

It can be seen that as the slope of the hill becomes steeper, the velocity profiles for the WRF and IBM-WRF solutions show more differences, especially in the lee of the hill. These differences are quantified in tables 3 and 4 for the two different aspect ratios. To directly compare the WRF and IBM-WRF solutions, the two solutions are interpolated onto a common time invariant terrain-following grid. This new grid uses the same horizontal spacing as the computational grid, however, the vertical grid spacing is independent of the grid for the solution. The IBM solution is subtracted from the WRF solution for each variable. The domain average of the difference, as well as the maximum difference is included in each table. For comparison, the domain averaged magnitude of each velocity component is also included in the table for the WRF and IBM-WRF solutions. It can be seen that the differences between the WRF and IBM-WRF solutions increase with increasing slope, for all velocity components in both the domain averaged and max norm differences. This trend holds for both aspect ratios. With a 10 degree slope and an aspect ratio of 2, the maximum difference between the IBM-WRF and WRF solutions for u velocity is 0.1455 m s^{-1}, which is just 1.5% of the domain averaged magnitude of 9.3042 m s^{-1} for u in the IBM-WRF domain. With a 30 degree slope, the difference increases to 1.9825 m s^{-1}, which is a 21.7% difference.

An additional result is that the differences between the IBM-WRF and WRF solutions are much larger for the grid with an aspect ratio of 1 than 2. Again for the u velocity component, with a 10 degree slope the maximum difference between the two solutions is 1.0395 m s^{-1} or 11.2%, while for a 30 degree slope the maximum difference is 3.1108 m s^{-1} or 34.0%. Increased error with a grid aspect

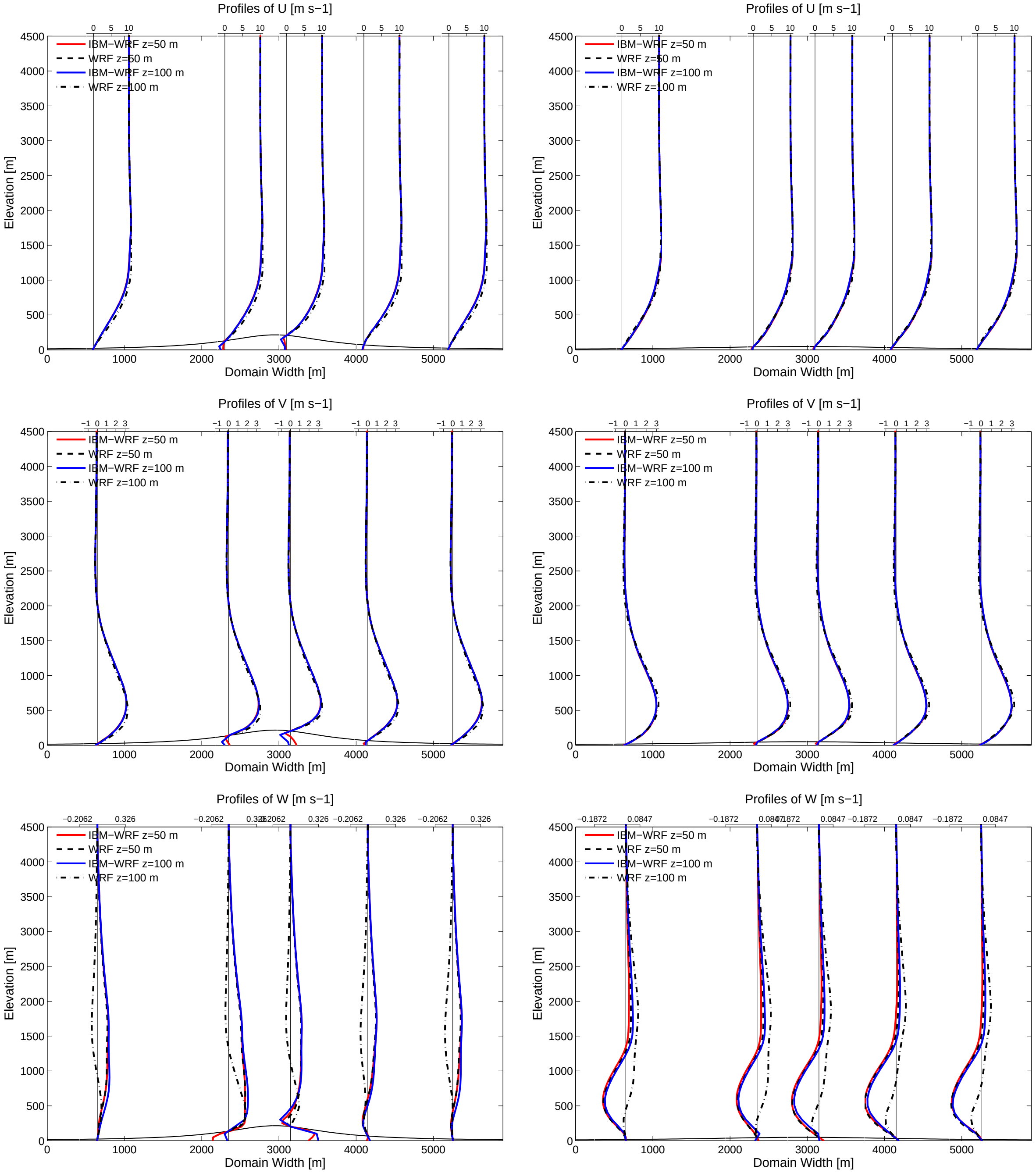

Figure 9: Profiles of u, v, and w velocity are shown for two horizontal locations located along a slice in the y dimension for a hill with a 10 degree slope. Profiles are located at $y \approx 3000$ m on the left and $y \approx 4500$ m on the right. Two different aspect ratios are used, resulting in Δz = 50 m or Δz = 100 m.

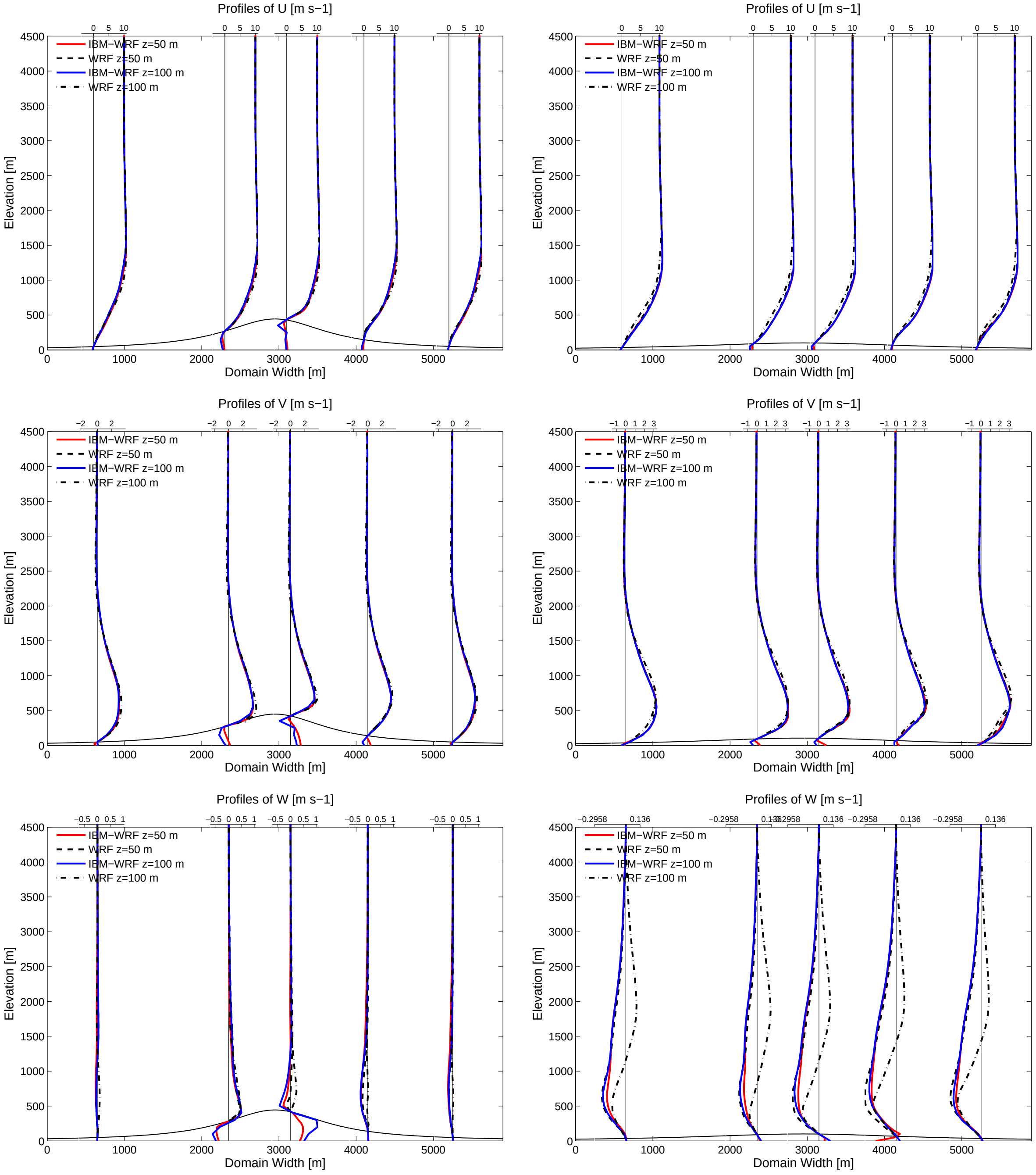

Figure 10: Profiles of u, v, and w velocity are shown for two horizontal locations located along a slice in the y dimension for a hill with a 20 degree slope. Profiles are located at $y \approx 3000$ m on the left and $y \approx 4500$ m on the right. Two different aspect ratios are used, resulting in Δz = 50 m or Δz = 100 m.

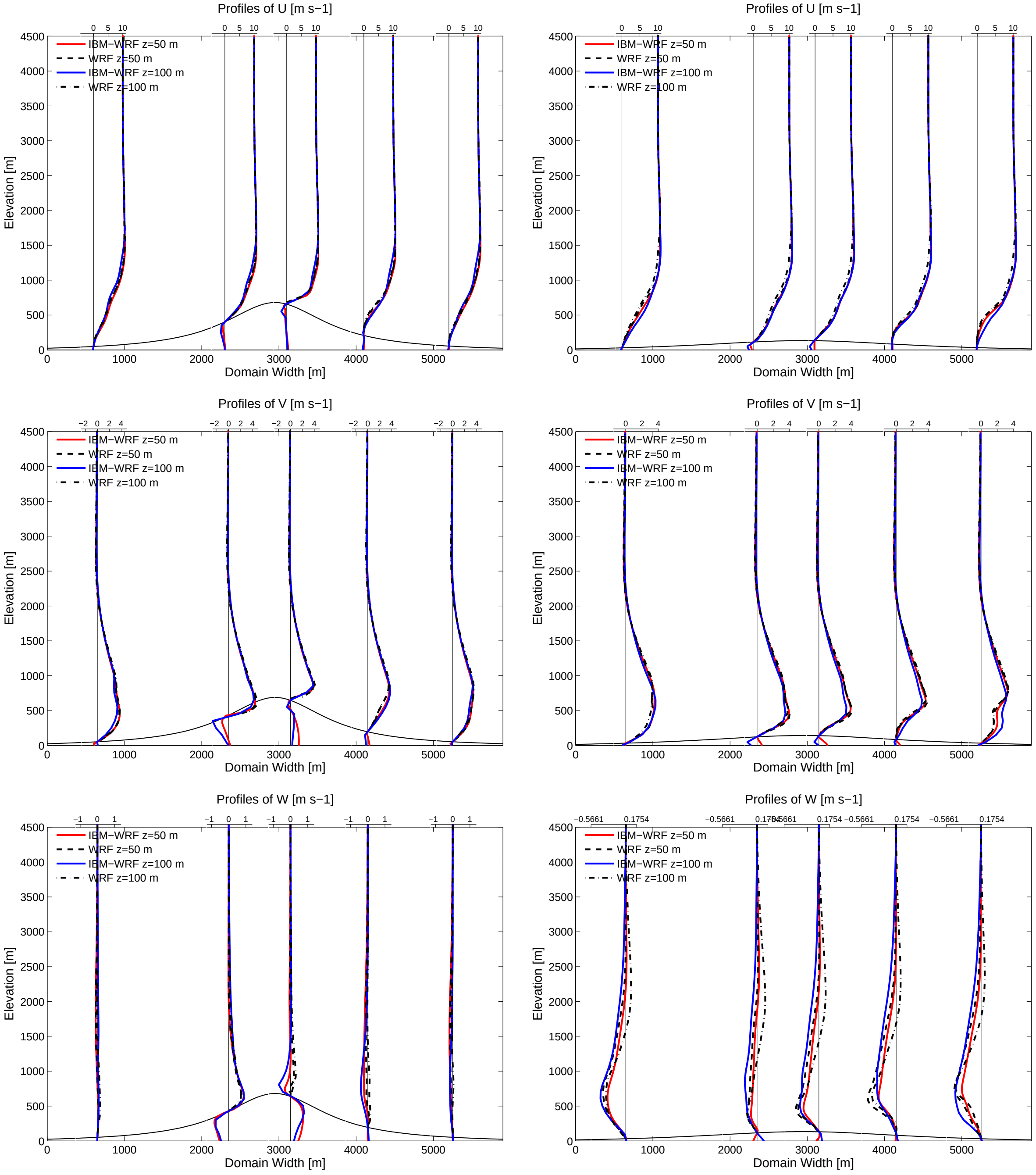

Figure 11: Profiles of u, v, and w velocity are shown for two horizontal locations located along a slice in the y dimension for a hill with a 30 degree slope. Profiles are located at $y \approx 3000$ m on the left and $y \approx 4500$ m on the right. Two different aspect ratios are used, resulting in Δz = 50 m or Δz = 100 m.

ratio of 1 is a somewhat unexpected result, as seen in figure 2, it is expected that a grid with an aspect ratio of 1 could handle steeper slopes than a grid with an aspect ratio of 2. It is likely that resolution or grid spacing is also an important quantity to consider here, and that the larger differences between the WRF and IBM-WRF solutions could be attributed to under-resolving velocity gradients in the vertical direction. More simulations at different resolutions and aspect ratios are needed to quantify the contribution to errors from grid aspect ratio.

Figure 12 plots the spatial differences in the IBM-WRF and WRF solutions by showing contours of velocity differences along the center line of the domain (coinciding with the peak of the hill). Here the differences in velocity magnitude are calculated as $\sqrt{u_{diff}^2 + v_{diff}^2 + w_{diff}^2}$. Contour and color bar levels are common for the three terrain slopes shown. From these plots, it is clear that not only do the differences between the two solutions increase as terrain slope increases, but the differences are also largest in the lower portion of the domain where grid skewness is largest. The largest differences are seen near the peak and in the lee of the hill. This is the region where the terrain effects the flow the most through speed-up over the peak and separation in the lee of the hill. Grid quality effects the regions with varying velocity profiles more than in the regions where the profiles or uniform or linear. This was demonstrated in the previous example of an atmosphere at rest.

As shown in equations 4 and 5, the Jacobian of the coordinate transformation appears in the truncation error term and can act in the same way that error from finite differencing does, meaning the coordinate transformation errors can create numerical diffusion which has a similar effect as viscosity. A simulation was performed with the viscosity increased to 30 m^2 s^{-1}, from the value of 20 m^2 s^{-1} used in the previous simulations. As viscosity increases, the actual viscosity becomes the dominate source of diffusion, rather than truncation error from the finite difference scheme and coordinate transformation. Figure 13 shows the differences in velocity between the IBM-WRF and WRF solutions, as in figure 12 for the two different viscosities. The differences in the solutions decrease with increased viscosity. As the behavior of the IBM is independent of the prescribed viscosity, this decrease in difference can be attributed to parameterized turbulent mixing becoming the dominant term over truncation error.

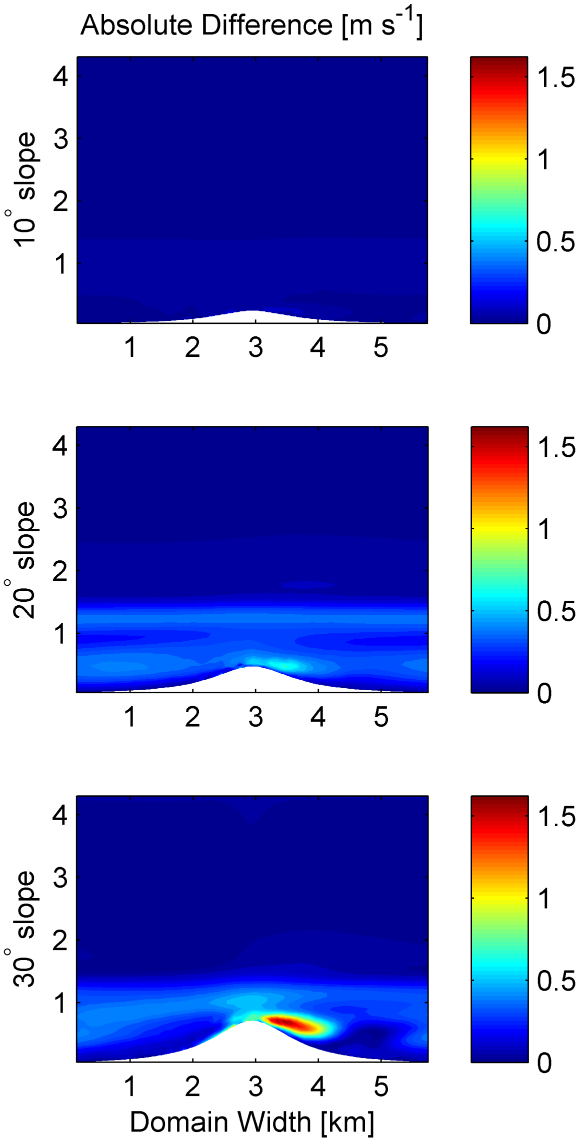

Figure 12: Difference between the IBM-WRF and WRF solutions for three different slopes (10, 20, and 30 degrees) along the center line of the domain and the peak of the hill. Contours are of the magnitude of the velocity differences, including all three velocity components. Contour levels and the color bar are held constant for all three terrain slopes.

Table 3: Domain averaged differences and velocity values for each velocity component for simulations with an aspect ratio of 2 (Δz = 50 m). The max norm for the difference over the entire domain is also included. All quantities have units of m s^{-1}.

		$\Delta\varphi_{ave}$	φ_{IBMave}	φ_{WRFave}	$\Delta\varphi_{max}$
10° slope	u	0.0119	9.3042	9.3038	0.1455
	v	0.0087	0.6943	0.6983	0.1327
	w	0.0047	0.0025	0.0023	0.0588
20° slope	u	0.0702	9.2488	9.2414	0.7303
	v	0.0328	0.7249	0.7266	0.4438
	w	0.0253	2e-4	0.0016	0.2132
30° slope	u	0.0684	9.1353	9.0947	1.9825
	v	0.0503	0.8214	0.8039	1.1865
	w	0.0221	3e-5	5e-4	0.5563

Table 4: Domain averaged differences and velocity values for each velocity component for simulations with an aspect ratio of 1 (Δz = 100 m). The max norm for the difference over the entire domain is also included. All quantities have units of m s^{-1}.

		$\Delta\varphi_{ave}$	φ_{IBMave}	φ_{WRFave}	$\Delta\varphi_{max}$
10° slope	u	0.1618	9.3164	9.3213	1.0395
	v	0.0806	0.6941	0.7002	0.6935
	w	0.0616	0.0025	-4e-4	0.1999
20° slope	u	0.2264	9.2674	9.2652	1.8113
	v	0.1089	0.7272	0.7285	1.4322
	w	0.0817	0.0013	0.0013	0.6472
30° slope	u	0.2268	9.1590	9.1216	3.1108
	v	0.1182	0.8121	0.8157	2.1768
	w	0.0814	0.0024	0.0029	0.9790

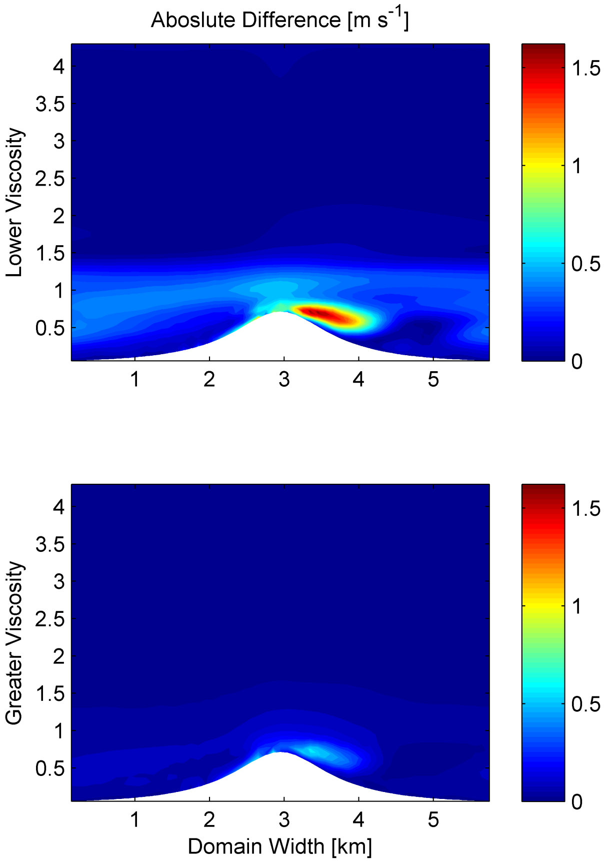

Figure 13: Difference between the IBM-WRF and WRF solutions for two different viscosities (20 and 30 m^2 s^{-1}) along the center line of the domain and the peak of the hill. Contours are of the magnitude of the velocity differences, including all three velocity components. Contour levels and the color bar are held constant for both subfigures.

4 CONCLUSIONS

Errors due to terrain-following coordinates have been quantified in three test cases: 2D scalar advection over topography, a 3D atmosphere at rest over an isolated hill, and forced advection over a 3D hill. In each of the two idealized test cases with analytical solutions, errors disappeared almost completely in the IBM-WRF solution. Thus we were able to use IBM-WRF as a reference for comparison in a more complex 3D flow without an analytical solution. As the errors with terrain-following coordinates are caused by poor grid quality, especially considering properties such as aspect ratio and the orthogonality of coordinate surfaces or skewness of grid cells, we also sought to quantify the effects of these grid properties by varying these parameters and directly comparing the WRF and IBM-WRF solutions. When the quality of the terrain-following solution deteriorates, the accuracy of the solution benefits from using the immersed boundary method instead. From our simulations, it is clear that error from the terrain-following grid increases with increasing slope, while the immersed boundary method is an effective tool for eliminating error at any slope. The error in the terrain-following grid can be substantial, even with slopes as shallow as 10 degrees, depending on the quality of the grid and the specifics of the problem being simulated (such as discontinuities in the solution). While it was clear from our simulations that grid aspect ratio and resolution also contribute to the accuracy of the solution (especially with terrain-following grids) more simulations are needed to provide specific recommendations on when the use of terrain-following grids is acceptable and when the immersed boundary should be used.

5 ACKNOWLEDGEMENTS

The first author gratefully acknowledges the Lawrence Scholars program at Lawrence Livermore National Laboratory. The second author acknowledges the support of National Science Foundation grant ATM-0645784. This work was performed under the auspices of the U.S. Department of Energy by Lawrence Livermore National Laboratory under Contract DE-AC52-07NA27344.

REFERENCES

A. Adcroft, C. Hill, and J. Marshall. Representation of topography by shaved cells in a height coordinate ocean model.

Mon. Weather Rev., 125:2293–2315, 1997.

T. Gal-Chen and R.C.J. Somerville. On the use of a coordinate transformation for the solution of the navier-stokes equations. *J. Comp. Phys.*, 17:209–228, 1975.

G. Iaccarino and R. Verzicco. Immersed boundary technique for turbulent flow simulations. *Appl. Mech. Rev.*, 56:331–347, 2003.

Z.I. Janjić. Pressure gradient force and advection scheme used for forecasting with steep and small scale topography. *Beitr. Phys. Atmos.*, 50:186–189, 1977.

Z.I. Janjić. On the pressure gradient force error in σ coordinate spectral models. *Mon. Weather Rev.*, 117:2285–2292, 1989.

J.B. Klemp, W.C. Skamarock, and O. Fuhrer. Numerical consistency of metric terms in terrain-following coordinates. *Mon. Weather Rev.*, 131:1229–1239, July 2003.

D. Lee and Y.M. Tsuei. A formula for estimation of truncation errors of convective terms in a curvilinear coordinate system. *J. Comp. Phys.*, 98:90–100, 1992.

K.A. Lundquist, F.K. Chow, and J.K. Lundquist. An immersed boundary method for flow over complex terrain. In *13th Conference on Mountain Meteorology*, page 10, Whistler, BC, 2008. American Meteorological Society. [Paper 9A.5].

K.A. Lundquist, F.K. Chow, and J.K. Lundquist. An immersed boundary method for the Weather Research and Forecasting model. *Mon. Weather Rev.*, 138(3):796–817, 2010.

Y. Mahrer. An improved numerical approximation of the horizontal gradients in a terrain-following coordinate system. *Mon. Weather Rev.*, 112:918–922, 1984.

R. Mittal and G. Iaccarino. Immersed boundary methods. *Annu. Rev. Fluid Mech.*, 37:239–261, 2005.

R.A. Pielke. *Mesoscale Meteorological Modeling*. Academic Press, Inc., 1984.

C. Schär, D. Leuenberger, O. Fuhrer, D. Lüthi, and C. Girard. A new terrain-following vertical coordinate formulation for atmospheric prediction models. *Mon. Weather Rev.*, 130: 2459–2480, October 2002.

D. You, R. Mittal, M. Wang, and P. Moin. Analysis of stability and accuracy of finite-difference schemes on a skewed mesh. *J. Comp. Phys.*, 213:184–204, 2006.

G. Zängl. An improved method for computing horizontal diffusion in a sigma-coordinate model and its application to simulations over mountainous topography. *Mon. Weather Rev.*, 130:1423–1432, 2002.

G. Zängl. A generalized sigma-coordinate system for the mm5. *Mon. Weather Rev.*, 131:2875–2884, 2003.

G. Zängl, L. Gantner, G. Hartjenstein, and H. Noppel. Numerical errors above steep topography: A model intercomparison. *Meteorol. Z.*, 13:69–76, 2004.